Interface Strain Induced Hydrophobic Facet Suppression in Cellulose Nanocomposite Embedded with Highly Oxidized Monolayer Graphene Oxide

Qian Mao, Lei Yang, Xiumei Geng, Liao Chen, Bedanga Sapkota, Huijuan Zhao,* and Hongli Zhu*

In nature, cellulose is a unique lightweight biopolymer with outstanding mechanical and optical properties that is readily available. Rigorous investigations have been conducted to use cellulose as an ingredient in the advanced functional composite design. In this work, a hybrid film composed of homogeneous cellulose nanocrystals (CNC) and high oxidation graphene oxide (GO) is obtained by sufficient blending and vacuum filtration. For the first time through the X-ray diffraction (XRD) spectrum, the suppression of the originally ordered hydrophobic (200) facet of CNC is observed with increasing concentrations of GO. Further, the originally ordered hydrophilic (110)/(1-10) facets of CNC remain intact. Through systematic molecular dynamics simulations of a set of simplified CNC–GO sandwich structures, the mechanism behind this hydrophilic/hydrophobic facets manipulation is revealed. The strain induced by the hydrogen bonding between the CNC hydroxyl groups and the oxidation types on GO is the dominant reason to cause the suppression of the hydrophobic facet of CNC in CNC–GO hybrid film. This strain induced mechanism provides an understanding for intrinsically manipulating cellulose–matrix interface and potentially engineering the cellulose based nanocomposite material properties for future advanced materials development.
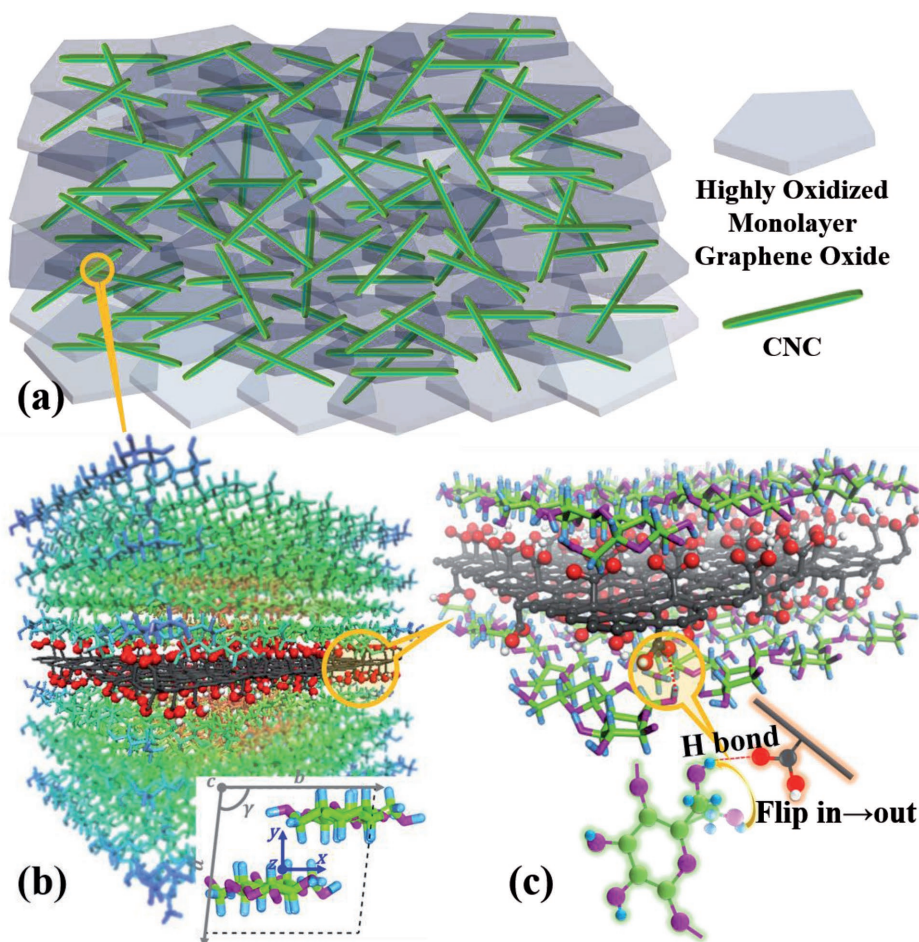
1. Introduction

As the most abundantly available raw material on earth, cellulose is a carbohydrate biopolymer with desired material properties.[1–3] As an essential unit of the native cellulose fibers, cellulose elementary fibrils are formed by single-molecule chains consisting of a linear polymer chain of anhydro-D-glucose via β-1-4 linkage.[4–6] These cellulose microfibrils contain both disordered amorphous regions and well-ordered crystalline domains. After the total hydrolysis of disordered amorphous regions, the residual of well-ordered crystalline sections are known as cellulose nanocrystals (CNCs).[9–11] Among the various allomorphs of cellulose nanocrystals, Young's modulus is calculated varying between 10.3 GPa (amorphous)[13] and 130 GPa (crystalline).[7,2,12] The abundance, novel mechanical properties, and low density (≈ 1.59 g cm^{-3}) have made CNC a desirable biopolymer reinforcement component for the use of lightweight and superstrong nanocomposite materials.[8]

In a nanocomposite, the fiber–fiber bonding and fiber–matrix adhesion are the dominant factors in determining the structures and properties of the material. The reinforcing effect of CNC is mainly due to the hydrogen bond formation among the CNC–CNC fibers and CNC–matrix. Various strategies have been adopted to modify the hydrophobicity of CNC in order to achieve desired interface bonding between the CNC reinforcements and the matrix.[14–16] In this study, for the first time, we experimentally demonstrated the suppression of (200) facet of CNC within a nanocomposite film composed of homogeneous cellulose nanocrystals (CNC) and highly oxidized monolayer graphene oxide (GO), as shown in **Scheme 1**a. The highly crystalized CNC was decomposed from the microfibrils of wood, which are assembled with ≈ 36 individual cellulose molecule chains bonded with each other through hydrogen bonds. The highly oxidized monolayer graphene oxide was selected as the counterpart material to introduce more fiber–matrix interaction in the nanocomposite film. The reason we choose highly oxidized graphene oxide in this study is that there are a lot of functional group, —OH and —COOH, at the graphene oxide surface and make it super hydrophilic. From the XRD spectrum, we found the suppression of (200) facet and shift of (110) and (1-10) facets of CNC. With the substantial amount of hydroxyl (—OH) and carboxyl (—COOH) groups on the graphene oxide, we think that there is a strong association between the (200)

Q. Mao, Dr. H. Zhao
Department of Mechanical Engineering
Clemson University
Clemson, SC 29634, USA
E-mail: hzhao2@clemson.edu
L. Yang, Dr. X. Geng, L. Chen, Dr. H. Zhu
Department of Mechanical Engineering
Northeastern University
Boston, MA 02115, USA
E-mail: h.zhu@neu.edu
Dr. B. Sapkota
Department of Physics
Northeastern University
Boston, MA 02115, USA

ADVANCED
SCIENCE NEWS
www.advancedsciencenews.com

ADVANCED
MATERIALS
INTERFACES
www.advmatinterfaces.de

Scheme 1. a) The CNC–GO nanocomposite film with uniformly distributed CNC nanorods and highly oxidized monolayer graphene oxide nanoflakes. b) The cellulose–GO–cellulose sandwich model in MD simulation with the unit cell of the Iβ cellulose in the subfigure. c) The −OH flipping mechanism at the cellulose–GO interface. In this scheme, carbon, hydrogen, and oxygen atoms on cellulose are presented in green, blue, and purple, respectively; carbon, hydrogen, and oxygen atoms on GO are presented in dark grey, white, and red respectively. The flipping "in→out" means the functional groups are flipping toward the GO interface.

facet suppression and the hydrogen bonds formed at the CNC–GO interface during the preparation of nanocomposite film.

To gain the insight into the mechanism responsible for the vanishing (200) peak, we selected a CNC–GO interface in the nanocomposite and performed the classical molecular dynamics (MD) simulations to systematically investigate the cellulose–GO interface interaction, shown in Scheme 1b. By considering various cellulose orientations, thicknesses and GO oxidation types in this simplified sandwich structure, we found that the GO interaction with CNC (200) and (110) facets in the form of hydrogen bonds can lead to various levels of distortion of the CNC lattice, causing the variations of the lattice vectors and lattice configurations, therefore leading to the peak shifting and peak weakening in the XRD profile. More specifically, the hydrogen bonding between GO and cellulose (200) plane can significantly induce the weakening and shifting of the (200) peak in the XRD profiles. The hydrogen bonding between GO and cellulose (110) interface only causes the (110) and (1-10) peaks to shift closer to each other in the XRD profiles, without significantly affecting the (200) peak intensity and location.

Through the MD simulations, we also demonstrate that at the GO–cellulose (200) interface, the −COOH functional groups on GO can trigger more −OH functional groups from the cellulose (200) interface to flip toward the GO surface (flip-out), as shown in Scheme 1c. Such interaction can cause the alternating twisting among glucose rings along the cellulose chain direction, which is identified to be the main reason of the (200) peak weakening through the theoretical morphology investigation of the cellulose crystal structure.

2. Results and Discussion

The experimental details are introduced in the Methods section. Highly oxidized and single-to-few layer graphene oxide was first mixed with the CNC in solution with different ratios for 72 h and followed by vacuum filtration to form the nanocomposite film. As shown in inset in **Figure 1**a and Figure S1a (Supporting Information), the obtained film is smooth, flexible, and uniform in thickness (≈10 μm). Within the scanning
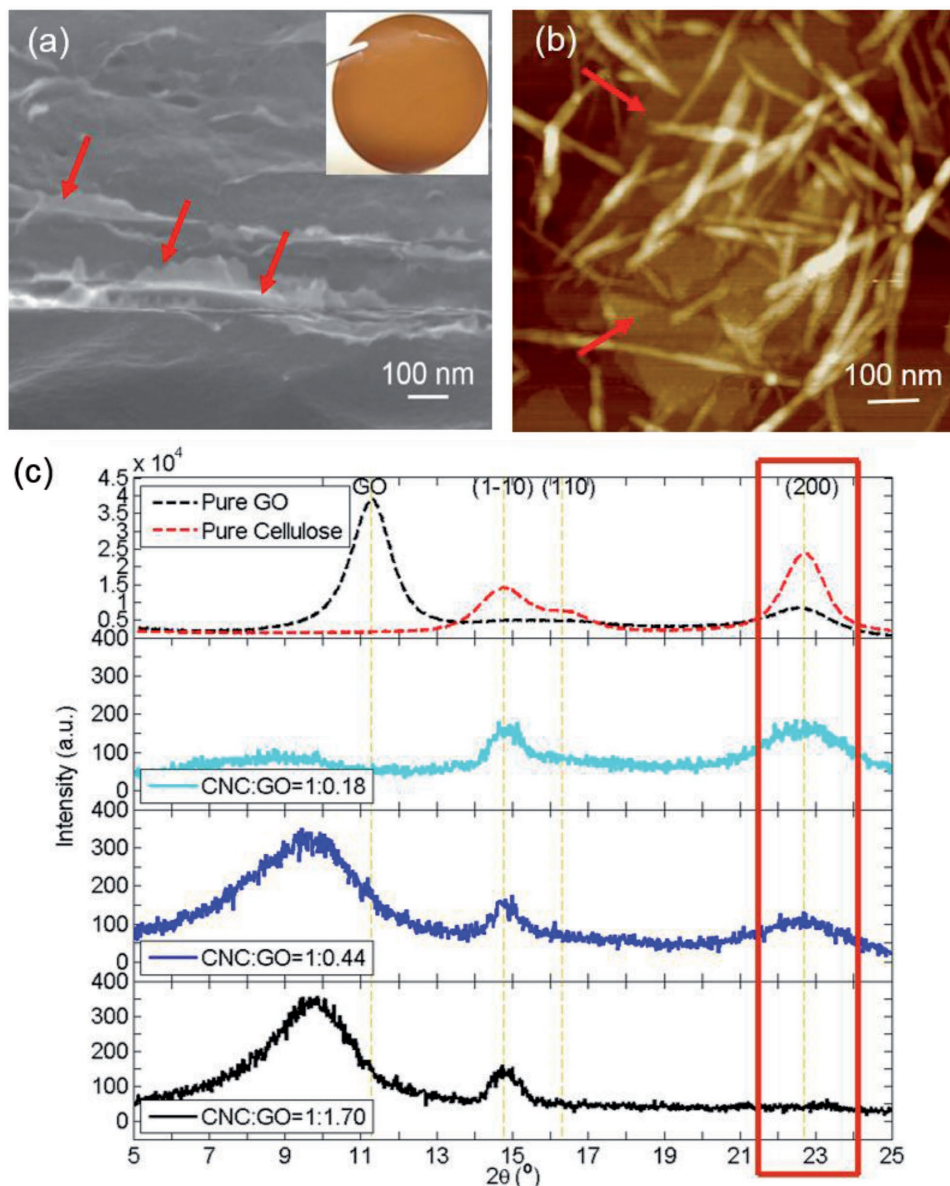
Figure 1. The characterization of the GO/CNC composite film. a) SEM image of the cross-section of the composite film with the red arrows indicating the monolayer of GO nanosheets, and the inset photograph shows the uniform GO/CNC hybrid film; b) AFM image of the composite film surface with the randomly embedded CNC fibers and GO nanosheets, with the red arrows indicating the monolayer of GO nanosheets; c) XRD spectrum of pure GO (black dash), pure CNC (red dash), and the composite films with various CNC:GO ratios.

electron microscope (SEM) image of the composite film cross-section in Figure 1a and Figure S1b (Supporting Information), a clear layer-by-layer structure can be observed, that contains 2D monolayer GO nanosheets (as indicated by the red arrows in Figure 1a) and uniformly distributed CNC fibers in between. The surface morphology of the composite film at the nanoscale was observed with atomic force microscopy (AFM) in Figure 1b, from which the hybrid materials of CNC nanorods and monolayer GO nanosheets, shown by the red arrows in Figure 1b. X-ray diffraction (XRD) spectrum was performed to visualize the atomic and molecular structure of the crystalline domain in CNC, GO, and CNC/GO mixture with weight ratios from 1: 0.18 to 1: 1.70. As presented in Figure 1c, the

XRD diagram of the CNC shows three diffraction peaks at $2\theta = 14.7°$, $15.9°$, and $22.7°$, which are the characteristics of cellulose crystal assignments of the (1-10), (110), and (200) planes, respectively.[17] The crystallinity index (CrI) was calculated at 89.70% using the empirical Segal equation.[18,19] Interestingly, while the (110) facet remains, the (200) facet is weakened with the increase of GO: CNC ratio, which indicates that the originally ordered (200) facet (−CH−) arrangement is disrupted with the increase of GO concentration. At the same time, the (200) peak of GO shift from $2\theta = 11.3°$ to $2\theta = 9.8°$ due to larger layer space expanded by the interaction with cellulose.[18]

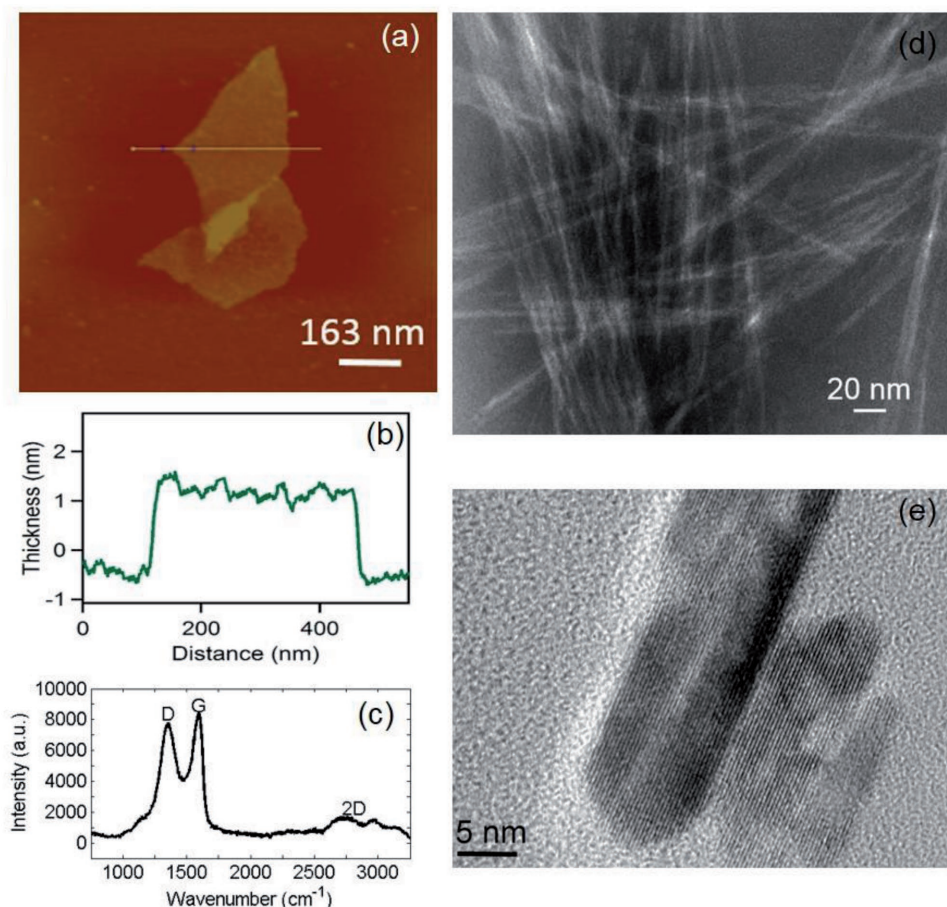Morphology observation is the most direct method used to characterize the interaction between CNC nanorods and

**ADVANCED
SCIENCE NEWS**
www.advancedsciencenews.com

**ADVANCED
MATERIALS
INTERFACES**
www.advmatinterfaces.de

Figure 2. Characterization of GO and CNC. a) AFM image of GO; b) the corresponding line scan of GO in (a); c) Raman spectrum of pure GO; d)TEM image of CNC; e) HRTEM image of CNC.

monolayers of GO nanosheets. A low concentration of highly oxidized GO (see Methods) was dropped onto a newly exfoliated surface of mica and then analyzed by AFM, as shown in **Figure 2**a. The prepared GO nanosheets were dispersed in water very well with no aggregation. The planar size of the GO is ≈150–200 nm, and the corresponding height profile is ≈1.1 nm, indicating a complete exfoliation of graphene oxide to a single to few layer, shown in Figure 2b. Through Raman spectroscopy, we observed that the GO showed a D band at 1344 cm^{-1} and G band at 1600 cm^{-1} respectively (Figure 2c). The intensity ratio, 0.92, of the D and G band (I_D/I_G) indicates a percentage of defects and disorder presented in the GO. Meanwhile, we observed a significant feature and intensity of 2D bands located between 2600 and 3000 cm^{-1} in the Raman spectrum, from which we conclude that a certain percentage of synthesized graphene oxide is a monolayer. The morphology of the prepared CNC (see Methods) is characterized with transmission electron microscope (TEM), shown in Figure 2d. The average diameter of the CNC nanorods is ≈3–10 nm with a length of ≈100–200 nm. The high-resolution TEM (HRTEM) image presented in Figure 2e well illustrates the ordered crystalline pattern in the CNC. As illustrated in Figure 1b the highly crystalline CNC nanorod was uniformly mixed with highly oxidized GO nanosheets to form hydrogen bonds, through which

the two building blocks interact with each other at the interface to change the arrangements of the CNC chains. The Fourier transform Infrared (FTIR) spectroscopy data in Figure S2 (Supporting Information) showed that the GO exhibits the characteristic broad band at 3300 cm^{-1} that corresponds to the stretching vibrations of bonded −OH. The peak at 1720 cm^{-1} corresponds to the C=O stretching vibration, while the peak at 1620 cm^{-1} is sometimes assigned to the −OH vibrations due to the presence of adsorbed water. The representative spectrum of cellulose was obtained with strong peaks at 3400–3500 cm^{-1} and 1620 cm^{-1}, which corresponds to −OH stretching and bending vibrations, respectively.

The peak at 2900cm^{-1} was assigned to −CH stretching vibration, which just appeared in the pure CNC film. The peaks at 1430cm^{-1} and 1335 cm^{-1} correspond to the symmetric bending of −CH$_2$ groups and the bending vibration of −CH groups. In the CNC and GO nanocomposite film, the −C−O−C− stretching vibration appears at 1045 cm^{-1}.

The Iβ CNC elementary fibril is commonly interpreted to contain the hydrophilic planes ((110) and (1-10)),[34] and the hydrophobic ((200)) plane.[35] For a typical CNC cross-section with ≈36 individual cellulose molecule chains, these cellulose molecule chains are arranged periodically by following the unit cell shown in the subfigure of Scheme 1b. Specifically,

8 layers of cellulose molecule chains are present perpendicular to the (200) plane, 7 layers and 6 layers perpendicular to the (110) plane and (1-10) plane respectively.[29] In order to investigate the interaction between GO and each individual set of CNC surfaces, we performed the classical MD simulations (see Methods) by adopting a sandwich structure which contains the alternating cellulose slabs (with various facet orientations and thicknesses) and the monolayer graphene oxide (with single type of oxidation functional groups), shown in Scheme 1b. Note that the objective of MD simualtions is to adopt the simplified interface model to distinguish the hydrogen bonding effect to the variation of (200) and (110) peak locations and intensities in the XRD spectrum with respect to the cellulose orientation, cellulose slab thickness and GO oxidation type. The XRD spectrums of GO interaction with cellulose (200) facet slab and cellulose (110) facet slab from MD simulations are plotted in **Figure 3**a,b, respectively. The corresponding cellulose:GO molecular weight ratios are listed in the Table ST1 (Supporting Information). When the cellulose (200) facet interacts with GO, the cellulose–GO interface distance is slightly different from the two cellulose (200) layers' distance. Shown in Figure 3a, the (200) peak splits from $2\theta = 22.9°$ in the pristine cellulose case to a range of $2\theta = 20.5°$–23.5° in the sandwich models with different intensity depending on the GO oxidation type. The split peak near $2\theta = 22.9°$ dominates when cellulose (200) facet interact with GO–COOH, while the split peak near $2\theta = 21.0°$–22.0° dominates when cellulose (200) facet interact with GO–OH. With the decreasing cellulose slab thickness, the difference between two (200) peaks increases. On the other hand, the (1-10) peak and (110) peak slightly shift away from each other with no noticeable weakening with the decreasing cellulose slab thickness, regardless of the GO oxidation type. In Figure 3b,

the interaction between the surface of the cellulose slab (110) and GO cannot cause the significant weakening and shifting of the (200) peak in the corresponding XRD spectrums. However, the (110) peak and (1-10) peak significantly shift toward each other with the decreasing of the cellulose slab thickness, regardless of the GO oxidation type.

Figure 3 shows that the splitting, weakening and shifting of the XRD peaks are greatly related with the cellulose interfaces, GO oxidation types and cellulose slab thickness. These findings differ from the experimental observation shown in Figure 1c mainly due to the high crystallinity of the cellulose slab and the simplicity of the single type cellulose–GO interface involved in the computational model. However, we can still gain the insight into the mechanism behind the (200) peak suppression shown in Figure 1c. To be more specific, we propose the following hypotheses: the (200) peak weakening observed in the experiments is mainly due to the interaction between the GO and the CNC hydrophobic (200) facets; the remaining (110) peak is mainly due to the interaction between the GO and the CNC hydrophilic (110)/(1-10) facets. The −COOH and −OH groups on GO both have different roles during the interaction with the CNC (200) facet. In the following discussion, further investigation on the conformation variations of cellulose slabs in Scheme 1b are conducted to prove these hypotheses.

For any crystalline lattice, the location and intensity of the XRD peaks depend upon (1) the size and shape of the unit cell, which determine the relative positions of the diffraction peaks; and (2) the atomic positions within the unit cell, which determine the relative intensities of the diffraction peaks.[30] Based on the MD simulation results, we can provide a fundamental understanding about the XRD peaks splitting, shifting and weakening observed in Figure 3.
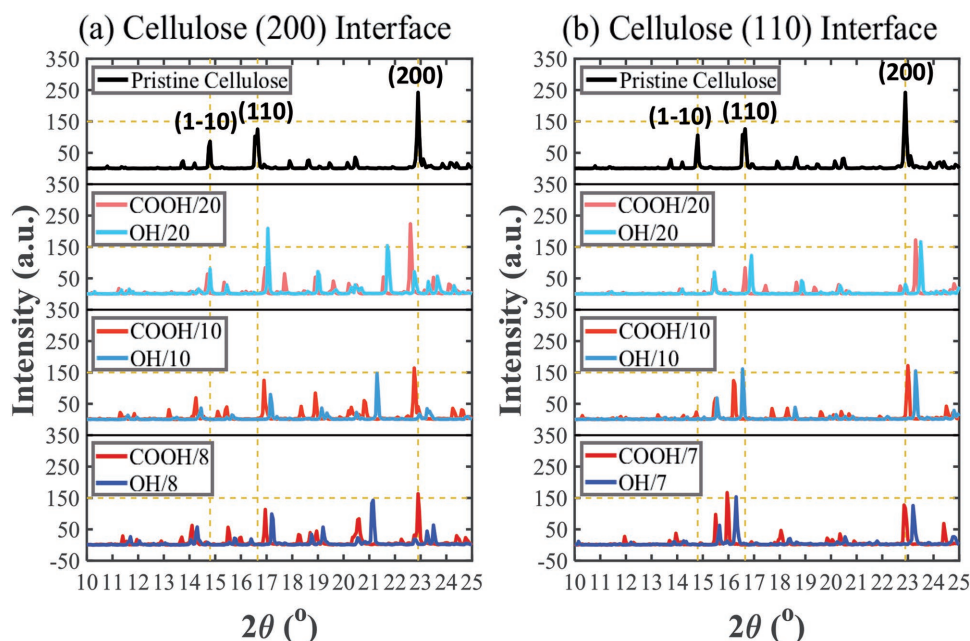

Figure 3. Simulated XRD spectrums with respect to the interface between GO and a) cellulose (200) facet and b) cellulose (110) facet. In each case, two GO oxidation types (−COOH and −OH) and three cellulose slab thicknesses are considered (20, 10, and 8 layers for cellulose (200) facet cases; 20, 10, and 7 layers for cellulose (110) facet cases). The legend represents the GO oxidation type and the number of layers along cellulose slab thickness direction, respectively. The corresponding cellulose:GO molecular weight ratios are listed in Table ST1 (Supporting Information).

**ADVANCED
SCIENCE NEWS**

www.advancedsciencenews.com

**ADVANCED
MATERIALS
INTERFACES**

www.advmatinterfaces.de

The Iβ cellulose crystal belongs to the monoclinic crystal lattice. The d-spacing $d_{(hkl)}$ in XRD spectrum can be evaluated as

$$\frac{1}{d^2} = \frac{1}{\sin^2 \gamma}\left[\frac{h^2}{a^2} + \frac{k^2}{b^2} + \frac{l^2 \sin^2 \gamma}{c^2} - \frac{2hk \cos \gamma}{ab}\right] \quad (1)$$

where d is the d-spacing; a, b, c, and γ are the lattice parameters; and h, k, and l are Miller index to define the crystalline plane (hkl). The 2θ can be evaluated through the Bragg's Law: $n\lambda = 2d \sin \theta$, where λ is the wave length of the X-ray, and n is an integer. Therefore, the location of (1-10), (110), and (200) peaks are mainly dependent on the magnitude of a, b, and γ, since l equals 0. Although the increase in both a and b can cause a leftward shift of (110) and (1-10) peaks, the increase in a can cause a large leftward shift of (200) peak whereas the variation of b cannot affect the location of (200) peak ($k = 0$). An increase in γ causes a leftward shift of the (1-10) peak, a rightward shift of the (110) peak, and leftward shift of the (200) at a smaller magnitude.

As observed in the MD simulations, a nonuniform strain field within the cellulose slab is developed due to the formation of hydrogen bonds at the cellulose–GO interface. As shown in **Figure 4**, the interface interaction between GO and cellulose slab (200) facet can increase the distortion of the cellulose lattice in a–b plane. However, it reduces the distortion of cellulose lattice under the interface interaction between GO and cellulose slab (110) facet. The lattice structure variation is more significant in the adjacent two layers at the GO–cellulose interface than the layers inside the cellulose slab. By analyzing

the averaged lattice parameter variation with respect to the cellulose orientations, the thicknesses and the GO oxidation types as shown in **Table 1**, we found that the cellulose (200) facet interaction with GO can enlarge the γ, and the interaction of the cellulose (110) facet with GO can reduce γ. The GO with −OH functional groups (denoted as GO–OH) can lead more elongation of the cellulose along a direction compared to the GO with −COOH functional groups (denoted as GO–COOH). Although the elongation along a direction can trigger the (200) peak shift in the XRD spectrum, such elongation is not uniformly distributed. The local elongation near the cellulose and GO interface is much larger compared to the local elongation developed at the center domain of the cellulose slab. The clear difference between the d-spacing near the cellulose–GO interface and the d-spacing near the center of cellulose slab lead to the bifurcation of the (200) peak shown in Figure 3a. Compared with the interaction between cellulose (200) and GO–-COOH, the interaction between cellulose (200) with GO–OH brings larger $d_{(200)}$ variation at the center domain of the cellulose (200). From Equation (1), each 0.29 ± 0.09 Å increase in $d_{(200)}$ can bring about a shift of $1.80° \pm 0.55°$ to the left in 2θ of the (200) plane XRD profile, and vice versa. Therefore, the enlarged $d_{(200)}$-spacing at the center domain of the cellulose (200) when interacted with GO–-OH can result in a high intensity (200) peak near 21°–22°, shown as the blue lines in Figure 3a. On the other hand, the (200) peak related with the center domain of cellulose (200) when interacted with GO–COOH remains near $2\theta = 22.9°$ and shifts a little to the right with the decreasing of the cellulose slab thickness, indicated by the red lines in
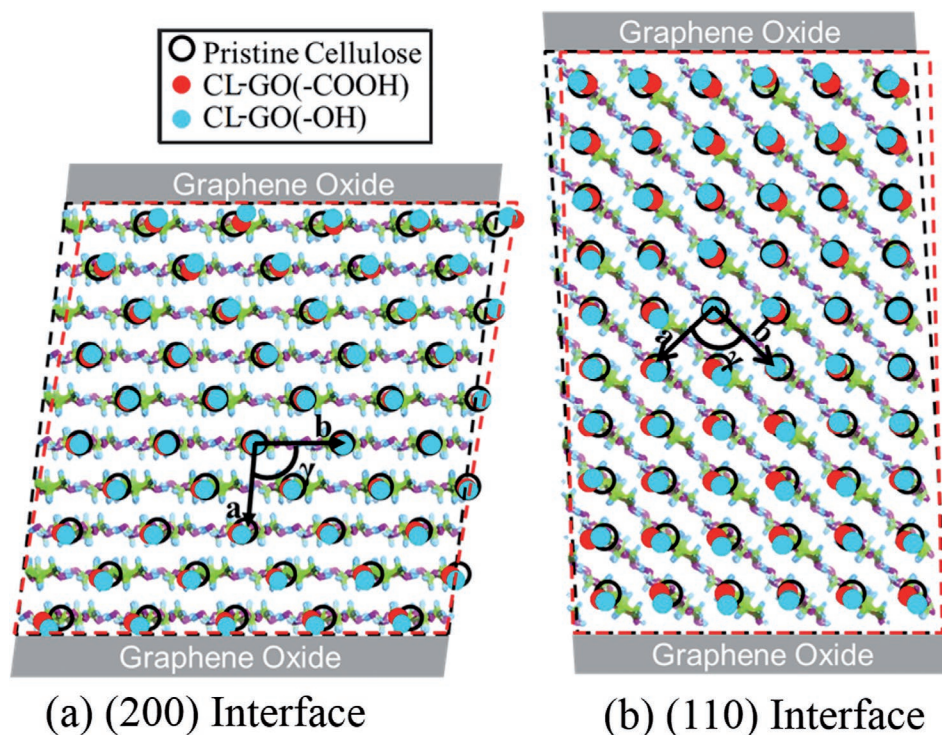

Figure 4. Deformation due to the interaction at the cellulose–GO interface. a) 10-layer-cellulose-slab with (200) facet interacted with GO; b) 10-layer-cellulose-slab with (110) facet interacted with GO. The circles and dots represent the centroid of each glucose ring. The black dash parallelogram represents the relaxed configuration without the GO interaction. The red dash parallelogram represents the relaxed configuration due to the interaction with GO containing −COOH functional groups.

**ADVANCED
SCIENCE NEWS**

www.advancedsciencenews.com

**ADVANCED
MATERIALS
INTERFACES**

www.advmatinterfaces.de

Table 1. Lattice parameter variations with respect to the cellulose face orientation, cellulose thickness and GO oxidation type.

	a [Å]	b [Å]	γ [°]	a [Å]	b [Å]	γ [°]
Reference[22,23]	7.78	8.20	96.50	7.78	8.20	96.50
Our work	7.65	8.09	96.40	7.65	8.09	96.40
	Cellulose (200) + GO–COOH			Cellulose (200) + GO–OH		
20 layers	7.85 ± 0.12	7.51 ± 0.12	97.92 ± 1.53	7.91 ± 0.12	7.45 ± 0.11	97.47 ± 1.52
10 layers	7.88 ± 0.17	7.54 ± 0.17	99.31 ± 2.15	7.93 ± 0.17	7.47 ± 0.15	98.39 ± 2.13
8 layers	7.90 ± 0.22	7.54 ± 0.23	99.53 ± 2.98	7.96 ± 0.18	7.46 ± 0.20	98.81 ± 2.93
	Cellulose (110) + GO–COOH			Cellulose (110) + GO–OH		
20 layers	7.50 ± 0.11	7.68 ± 0.14	95.36 ± 1.73	7.43 ± 0.11	7.74 ± 0.13	95.12 ± 1.44
10 layers	7.56 ± 0.14	7.64 ± 0.18	94.80 ± 1.97	7.51 ± 0.19	7.73 ± 0.22	93.92 ± 2.96
7 layers	7.56 ± 0.18	7.65 ± 0.21	94.58 ± 2.59	7.54 ± 0.31	7.91 ± 0.40	92.33 ± 6.05

Figure 3a. In order to further substantiate the nonuniform d-spacing distribution throughout the cellulose slabs, the MD and analytical 2θ values (from Figure 3 XRD spectrums and Equation (1), respectively) are tabulated in **Table 2** for comparison. By selecting proper integers for all Miller indices, the possible d-spacing values dominated at either near cellulose–GO interface or the center domain are derived by Equation (1). The 2θ values can be then calculated with the Bragg's Law. All splitting 2θ positions of (200) plane are found through the calculations, which are in good agreement with those of the MD. In conclusion, this analysis clearly shows that the cellulose–GO interaction impacts the characteristics of its XRD spectrum. More specifically, when cellulose slab is thin, the corresponding strain field induced by cellulose–GO interaction significantly affects the XRD spectrums.

The intensity of the diffraction peaks is determined by the periodicity of the atomistic structure within the unit cell, which can be estimated through Equations (2) and (3)[32]

$$F_{(hkl)} = \sum_n f_n \exp\left(2\pi i\left(hx + ky + lz\right)\right) \tag{2}$$

$$
\begin{aligned}
I_{(hkl)} &\propto F_{(hkl)} \cdot F_{(hkl)}^* \\
&= \sum_{m=1}^{3}\left[\left(\sum_n f_m \sin\left(2\pi\left(hx + ky + lz\right)\right)\right)^2 + \left(\sum_n f_m \cos\left(2\pi\left(hx + ky + lz\right)\right)\right)^2\right]
\end{aligned}
\tag{3}
$$

where $F_{(hkl)}$ is the structure factor which can be determined by the miller indices (hkl) and the fractional coordinates (x, y, z) over n atoms; f_n and f_m are atomic scattering factors determined by a nine-coefficient equation of Don Cromer and J. Mann;[33] $I_{(hkl)}$ is the crude peak intensity without correction factors, respectively. Through Equations (2) and (3), the (200) peak intensities can be estimated, as shown in the third and the sixth columns of Table 2. For instance, for the cases of cellulose interface (200) with −COOH/10 and −OH/10 in

Table 2. Comparisons between MD and analytical 2θ values as well as the analytical intensities (without corrections) of (200) peaks for all cases.

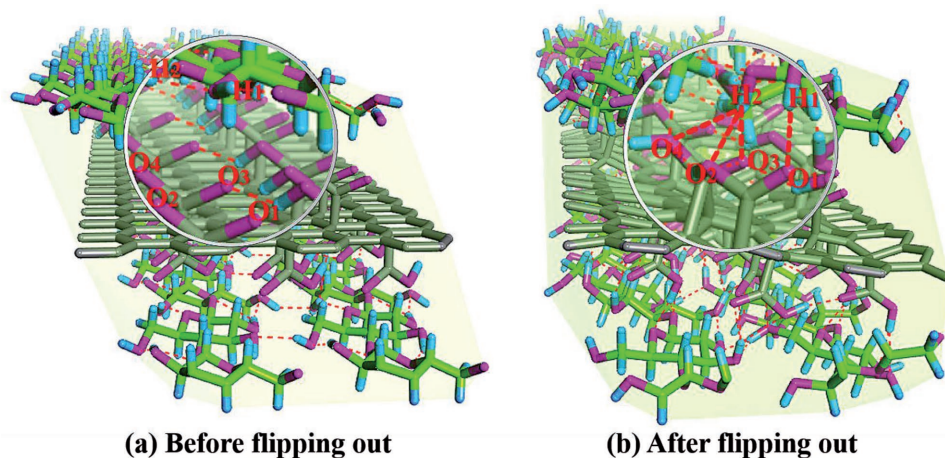|	Cellulose (200) + GO–COOH			Cellulose (200) + GO–OH		
	2θ [°] (MD)	2θ [°] (Analytical)	Intensity(10^8) (Analytical)	2θ [°] (MD)	2θ [°] (Analytical)	Intensity (10^8) (Analytical)
20 layers	21.55	21.55	1.65	21.70	21.72	6.78
	22.60	22.59	8.70	22.70	22.77	3.38
10 layers	20.80	20.82	0.66	21.30	21.30	2.11
	22.75	22.74	1.86	23.25	23.26	0.73
8 layers	20.60	20.57	0.51	21.15	21.12	1.43
	22.90	22.89	1.04	23.50	23.50	0.46
	Cellulose (110) + GO–COOH			Cellulose (110) + GO–OH		
	2θ [°] (MD)	2θ [°] (Analytical)	Intensity(10^8) (Analytical)	2θ [°] (MD)	2θ [°] (Analytical)	Intensity(10^8) (Analytical)
20 layers	22.70	22.70	1.75	22.90	22.88	2.24
	23.30	23.29	13.82	23.50	23.49	13.01
10 layers	21.90	21.90	0.12	22.20	22.18	0.23
	23.00	22.98	3.64	23.30	23.29	3.51
7 layers	–	21.43	0.01	–	21.73	0.03
	22.85	22.87	1.63	23.20	23.21	1.13

(a) Before flipping out   **(b) After flipping out**

Figure 5. Scheme 1 of the −OH flipping at the interface of cellulose (200) facet and GO with −COOH functional groups. The flipping "in → out" means the functional groups are flipping toward the GO interface. (a) Before cellulose −OH groups flip out, there are no hydrogen bonds (red dash lines) at cellulose–GO interface. (b) After cellulose −OH groups flip out, hydrogen bonds form at the cellulose–GO interface (donor H_1–acceptor O_1, donor H_2–acceptor O_2, donor H_2–acceptor O_3, and donor H_2–acceptor O_4, as shown in the figure).

Figure 3a, −COOH case shows higher intensity at 22.75° but lower intensity at 20.80° as opposed to the case of −OH. As discussed previously, the higher intensity of −COOH case at 22.75° is from the diffraction of smaller d-spacing near the center domain, with the lower at 20.80° caused by the weakening through more extensive conformational variations via the hydrogen bonds. In contrast, the −OH case has a larger d-spacing near the center domain, with a barely discernible powder diffraction at 23.25°, which instead accumulates the intensity at 21.30°. Meanwhile, with lower grade of disorganization at the interface, −OH case appears to have higher sum intensity from both 20.50° and 23.50° compared with the −COOH. In conclusion, the analytical intensity estimation without correction factors shown in Table 2 are quantitatively well matched with the XRD spectrum calculated from the MD simulation shown in Figure 3.

As emphasized in the previous section, the cellulose and GO interface interaction substantially affects the cellulose slab surface mophology near the interface. As shown in **Figure 5**, the hydrogen bonds between cellulose functional groups and GO functional groups mainly induce the strain field and morphology variation in the cellulose lattice, therefore affects the intensity of the associated XRD spectrums. We observed that when the −OH groups of cellulose are facing GO, their attached hydrogens can be easily trapped by the oxygen from −OH/−COOH groups on GO to form the hydrogen bonds. As shown in **Figure 6**, we analyzed the number of hydrogen bonds of both interlayers and intralayers of the 10-layer cellulose (200) cases and cellulose (110) cases. The cutoff distance of H-A (hydrogen–acceptor) is 2.8Å, with only a consideration of the strong hydrogen bonds, and the lower limit for the angle D-H-A (donor–hydrogen–acceptor) is 110°.[31] It is obvious that when cellulose (200) facet interacts with GO in Figure 6a, the interlayer hydrogen bonds are significantly redistributed between layers due to the cellulose–GO interaction, regardless of the functional group types on GO. The number of interlayer hydrogen bonds increases dramatically at the cellulose–GO interface, while constantly reduces in the

middle layers. However, the number of intralayer hydrogen bonds remain undisturbed within each (200) plane of cellulose throughout the slab thickness. When cellulose (110) facet interacts with GO shown in Figure 6b, the numbers of interlayer/intralayer hydrogen bonds gradually increase when approaching to the cellulose–GO interface. The number of intralayer hydrogen bonds reduces at the central layer of cellulose slab, while the number of interlayer hydrogen bonds remains unchanged. Because of the surface orientation, the (200) peak weakening in Figure 3 is associated with the interlayer hydrogen bonds when cellulose (200) facet interacts with GO, and the intralayer hydrogen bonds when cellulose (110) interacts with GO, which is consistent with our observation in Figure 6. For example, in Figure 6a, the extensive new formation of interlayer hydrogen bonds near the cellulose–GO interface causes the conformation change in rotamers[36] and alternates the glucose rings' twisting, which can weaken the (200) peak intensity.

In order to further understand the hydrogen bond formation at the cellulose–GO interface, we evaluate the dynamical variation of −OH and −COOH functional groups on cellulose slabs near the cellulose–GO interface, especially the relative positions of hydrogen atom. We define the hydrogen atom with initial position away from GO as "in," and toward to GO as "out." Therefore, "in → out" means hydrogen atom flips out toward GO surface; and "out → in" means hydrogen atom flips into the cellulose slab. As shown in **Figure 7**, for the hydrogen atoms attached to carbon atoms (−C−H), their flipping dynamics is maintained and balanced, regardless of the oxidation types on the GO and the orientations of the cellulose slab surface. However, for the hydrogen atoms from hydroxyl groups (−O−H), the interaction at the GO and cellulose slab face great affects the flipping dynamics, which significantly depends on the functional groups on GO and cellulose slab orientations. When the cellulose slab (200) facet is interacting with the carboxyl groups (−COOH) on GO, the flipping dynamics of hydrogen on the adjacent two layers of cellulose (200) slab at the cellulose–GO interface is unbalanced. More
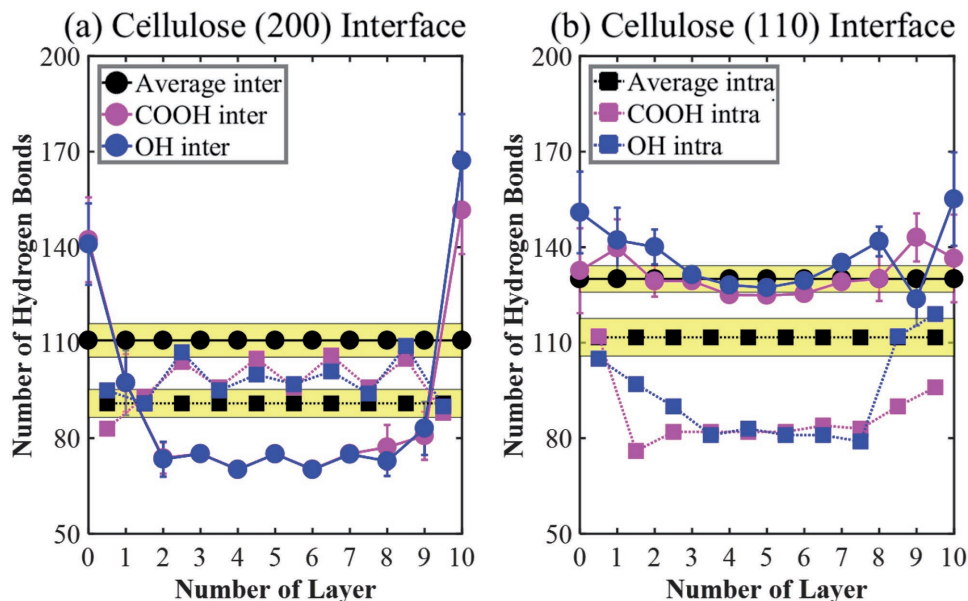
**ADVANCED
SCIENCE NEWS**
www.advancedsciencenews.com

**ADVANCED
MATERIALS
INTERFACES**
www.advmatinterfaces.de

Figure 6. Hydrogen bond variations with respect to the cellulose–GO interaction plane, GO functional group, and the location of the hydrogen bonding. The circular symbols represent the hydrogen bonding between either the cellulose/cellulose planes or the cellulose/GO planes (inter). The square symbols represent the hydrogen bonding within each cellulose plane (intra). The yellow domains represent the standard deviation of the average values of hydrogen bonds without GO interface interaction. Layers 0 and 10 for inter hydrogen bonds represent the number of hydrogen bonds between GO and the adjacent cellulose layers.

hydroxyl groups that are initially under the surface have been flipped out to interact with the carboxyl groups on GO. Therefore, the periodicity of the atomistic structures along the (200) plane is no longer maintained. Combined with the discussion about peak weakening in Table 2, the main reason responsible for (200) weakening shown as the magenta and red lines on Figure 3a is revealed.

3. Conclusion

In summary, hydrogen bond plays a dominant role in the CNC–matrix nanocomposite development. We experimentally observed the diminishment of cellulose (200) facet intensity in the XRD spectrum of CNC–GO nanocomposites with highly crystalline CNC and highly oxidized monolayer GO for the
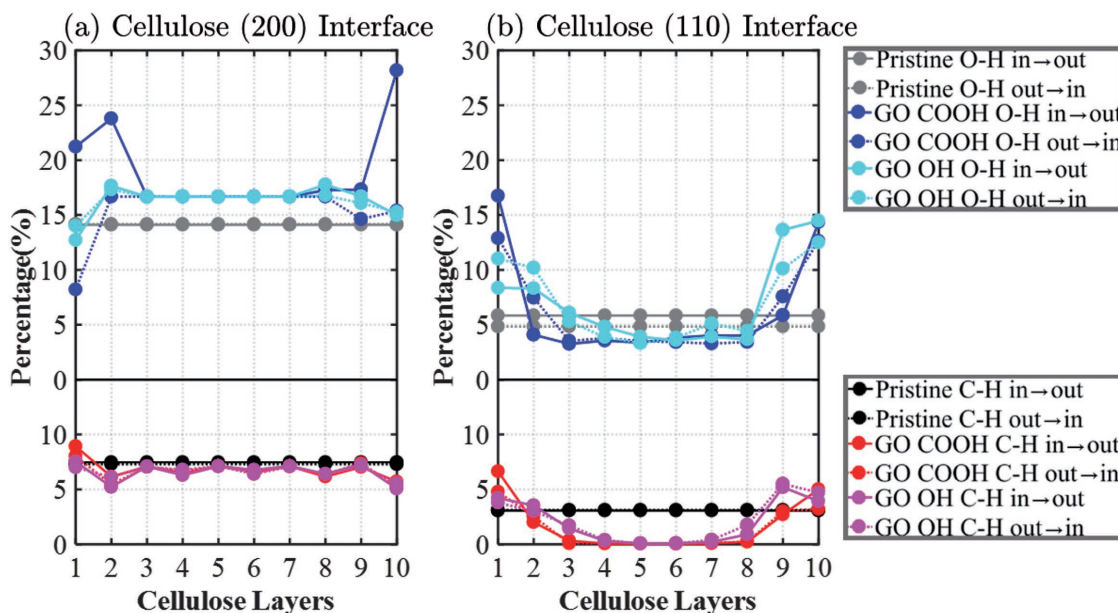

Figure 7. Hydrogen fliping on −OH and −COOH with respect to the cellulose–GO interface when cellulose slab is 10 layers thick. At both (200) and (110) interfaces, the hydroxyl group can be greatly flipped toward the cellulose–GO interface only when the GO–COOH interacts with the cellulose (200) surface.

**ADVANCED
SCIENCE NEWS**
www.advancedsciencenews.com

**ADVANCED
MATERIALS
INTERFACES**
www.advmatinterfaces.de

first time. Through the classical MD simulations, we identified the mechanism behind the hydrophilic/hydrophobic facets manipulation through systemic investigation on the effect of cellulose–GO interface interaction on the XRD spectrums with respect to the cellulose orientation and GO oxidation type. We observed that the hydrogen bonds at the cellulose–GO interface can induce a nonuniform strain field to the cellulose structure, including a global strain throughout the cellulose slab thickness and a local strain near the cellulose–GO interface. The interaction between the GO and cellulose hydrophobic (200) facet can largely cause broadening and weakening of the (200) peak. On the other hand, the interaction between GO and cellulose hydrophilic (110) facet can enhance the intensity of (1-10)/(110) peaks since the two peaks tend to shift close to each other. In regard to the oxidation type of GO, the −COOH functional groups affect the conformation of the cellulose (200) facet to a large extent due to the unbalanced −OH flipping dynamics. The insight of the reorganization of molecular orientation on interfaces is an essential prerequisite to understanding more multiple interactions that would involve ions, solvent, and, most interestingly, adsorption of abundant nanostructured materials. Meanwhile, this strain induced mechanism of crystalline structure alternation provides a methodology to intrinsically manipulating cellulose–matrix interface and potentially engineering the cellulose based nanocomposite material properties for future applications.

4. Experimental Section

Raw Material Resource: Cellulose microcrystalline was provided by Sigma-Aldrich Co. Ltd. Sulfuric acid (95–98%) for hydrolysis and regenerated cellulose dialysis tubing with a molecular weight cutoff of 12 000–14 000 were both purchased from Fisher Scientific. Graphite flake was purchased from Sigma-Aldrich Co. Ltd.

Highly Oxidized Graphene Oxide Preparation: 5 g of KNO_3 was first dissolved and stirred in 300 mL of concentrated H_2SO_4. Then, 2 g of natural flake graphite was slowly added to the above solution and stirred for 30 min. Afterward, the mixture was cooled to ≈0 °C using an ice bath and followed by slowly adding 30 g of $KMnO_4$ to the mixture solution. Temperature was closely watched during this process, and it was well-controlled under 20 °C. After the ice bath was removed, the reaction mixture was kept at 50 °C on a hot plate for 12 h. During oxidation, the color of the reaction mixture changed from dark purplish-green to dark brown, and the magnetic stirrer almost stopped spinning when a paste-like material was finally attained. The oxidation process was quenched and stopped by pouring the product to about 400 mL ice with strong stirring. Then 5 mL of 30% H_2O_2 was added. A golden-yellowish GO suspension was attained, which was stirred for another 30 min. Subsequently, the resulting precipitate was dialyzed using regenerated cellulose dialysis membranes having a molecular weight cutoff of 12 000–14 000 with deionized water until the wash water at constant PH. The product was centrifuged at 4000 rpm for one hour, and the supernatant was decanted. Then the remaining solid material was washed with water, 7% HCl, ethanol, and water sequentially. For each wash, the centrifugation was conducted at 4000 rpm for one hour. After the last wash, the supernatant was collected and further purified via dialysis for weeks before use.

Cellulose Nanocrystal Preparation: Cellulose microfiber was hydrolyzed at 45 °C for 4 h using 64 wt% sulfuric acid at an acid-to-cellulose of 10 mL g^{-1}. The hydrolysis reaction was quenched by dilution with tenfold water. The suspensions were washed with deionized water using repeated centrifuges. The supernatant was removed from the sediment

and replaced by new deionized. The centrifuge step was terminated until the supernatant became turbid. Subsequently, the resulting precipitate was dialyzed using regenerated cellulose dialysis membranes having a molecular weight cutoff of 12 000–14 000 Da with deionized water until the wash water at a constant PH. At last the samples were sonicated in an ice bath to avoid overheating.

Atomic Force Microscope Observation: GO imaging was undertaken at ambient temperature using fast scan dimension Atomic Force Microscope (Bruker, USA). A mica substrate was used for the sample preparation, and AFM was performed in the tapping mode of operation with a scan rate of 1.85 Hz using silicon cantilevers (force constant 18 N m^{-1}, resonance frequency 1400 kHz). Images were processed using Nanoscope software.

Transmission Electron Microscope Observations: TEM imaging and electron diffraction were performed on an FEI Tecnai G2 F20 S-Twin microscope operated at an accelerating voltage of up to 100 kV. The TEM sample was prepared ultrasonically at 500 W for ≈5 min, and 25 µL supernatant was dropped onto holey carbon grids.

Scanning Electron Microscopy Observations: Morphology of the as-prepared composite film was characterized by an ultrahigh resolution scanning electron microscope (Hitachi S4800). The film was first coated with 5 nm platinum and then imaged under ultrahigh resolution mode at 3 kV accelerating voltage to reveal the morphology.

X-Ray Diffraction Patterns: XRD patterns of GO and CNC were recorded for two theta values ranging from 4° to 60° in order to characterize the corresponding crystalline structure. The characterization was performed on a Bruker AXS-D8 Advance powder X-ray diffractometer using Cu/Kα radiation (λ = 1.5406 Å) with a step size of 0.02° and a dwell time of 3.0 s.

Fourier Transform Infrared Spectra: FTIR the GO suspension and the composite film were recorded using a spectrometer in the transmission mode over the range of 600–4000 cm^{-1} with a 4 cm^{-1} resolution for which the samples were dried on gold-coated silica substrate.

4.1. Modeling Section

Molecular Dynamics Simulations: Classical molecular dynamics simulations were undertaken to understand the interaction mechanism behind the cellulose–GO interface by using the large-scale atomic/molecular massively parallel simulator LAMMPS.[23–26] Since the average diameter of the CNC in the experiments is above 10nm, a sandwich structure containing an alternating pattern of the Iβ cellulose slab and GO monolayer was considered in a monoclinic simulation box. The objective is to understand the interaction between cellulose and GO interface with respect to the GO oxidation type, cellulose slab thickness, and cellulose surface orientation. With the convergence study of the atomic structure size, the simulation box was selected to be 4.10 nm in width and 5.19 nm in length, while the size along thickness direction was determined by the cellulose slab thickness. The in-plane strain, caused by a lattice mismatch at the cellulose slab and the GO interface can be eliminated. The oxidation ratio on graphene oxide was ≈44%, and the respective −OH functional and −COOH functional groups oxidation lattice structures were selected. To simulate the interaction among carbon, hydrogen, and oxygen atoms, the ReaxFF potential, which has been widely used for cellulose modeling, was adopted.[20–22] With a timestep of 0.5 fs, the relaxation of the system took ≈1 ns under the temperature of 100 K with the isothermal isobaric ensemble (NPT). The low-temperature 100 K was selected in order to achieve better statistics of the interface interaction without the complication due to the thermal dynamics within the simulation domain. We have performed some of the simulations at room temperature, the observation remains valid but with significant noises.[27,28] In order to investigate the cellulose slab thickness effect, we considered three thicknesses: 8 layers, 10 layers, and 20 layers for the cellulose (200) facet slabs; and three thicknesses: 7 layers, 10 layers, and 20 layers for the cellulose (110) facet slabs, respectively.

Supporting Information

Acknowledgements

Conflict of Interest

The authors declare no conflict of interest.

Keywords

[1] T. Huber, J. Müssig, O. Curnow, S. Pang, S. Bickerton, M. P. Staiger, *J. Mater. Sci.* **2012**, *47*, 1171.

[2] F. Dri, L. Hector, R. J. Moon, P. Zavattieri, *Cellulose* **2013**, *20*, 2703.

[3] U. G. K. Wegst, M. F. Ashby, *Philos. Mag.* **2004**, *84*, 2167.

[4] F. J. Kolpak, J. Blackwell, *Macromolecules* **1975**, *9*, 273.

[5] G. Nystrom, A. B. Fall, L. Carlsson, L. Wagberg, *Cellulose* **2014**, *21*, 1591.

[6] A. G. Dumanli, A. H. Windle, *J. Mater. Sci.* **2012**, *47*, 4236.

[7] A. Ishikawa, T. Okano, J. Sugiyama, *Polymer* **1997**, *38*, 463.

[8] *Properties and Performance of Natural-Fibre Composites* (Ed: K. E. Pickering), Elsevier, Boca Raton, FL, USA **2008**, p. *269*.

[9] D. Bondeson, A. Mathew, K. Oksman, *Cellulose* **2006**, *13*, 171.

[10] J. P. F. Lagerwall, C. Schütz, M. Salajkova, J. Noh, J. H. Park, G. Scalia, L. Bergström, *NPG Asia Mater.* **2014**, *6*, e80.

[11] Y. Habibi, L. A. Lucia, O. J. Rojas, *Chem. Rev.* **2010**, *110*, 3479.

[12] R. J. Moon, A. Martini, J. Nairn, J. Simonsen, J. Youngblood, *Chem. Soc. Rev.* **2011**, *40*, 3941.

[13] W. Chen, G. C. Lickfield, C. Q. Yang, *Polymer* **2004**, *45*, 1063.

[14] G. Siqueira, J. Bras, A. Dufresne, *Biomacromolecules* **2008**, *10*, 425.

[15] C. Bonini, L. Heux, J. Y. Cavaillé, P. Lindner, C. Dewhurst, P. Terech, *Langmuir* **2002**, *18*, 3311.

[16] P. Tingaut, T Zimmermann, F. Lopez-Suevos, *Biomacromolecules* **2009**, *11*, 454.

[17] S. Besombes, K. Mazeau, *Plant Physiol. Biochem.* **2005**, *43*, 299.

[18] M. Wada, L. Heux, J. Sugiyama, *Biomacromolecules* **2004**, *5*, 1385.

[19] L. Segal, J. J. Creely, A. E. Martin, C. M. Conrad, *Text. Res. J.* **1959**, *29*, 786.

[20] A. C. Van Duin, S. Dasgupta, F. Lorant, W. A. Goddard, *J. Phys. Chem. A* **2001**, *105*, 9396.

[21] X. Zhang, M. A. Tschopp, M. F. Horstemeyer, S. Q. Shi, J. Cao, *Int. J. Model., Identif. Control* **2013**, *18*, 211.

[22] J. A. Diaz, X. Wu, A. Martini, J. P. Youngblood, R. J. Moon, *Biomacromolecules* **2013**, *14*, 2900.

[23] S. Plimpton, P. Crozier, A. Thompson, *LAMMPS-Large-Scale Atomic/Molecular Massively Parallel Simulator*, Sandia National Laboratories, Albuquerque, New Mexico, USA **2007**, p. *18*.

[24] R. Rahman, J. T. Foster, A. Haque, *J. Phys. Chem. A* **2013**, *117*, 5344.

[25] B. D. Rabideau, A. Agarwal, A. E. Ismail, *J. Phys. Chem. B* **2013**, *117*, 3469.

[26] B. D. Rabideau, A. E. Ismail, *Phys. Chem. Chem. Phys.* **2015**, *17*, 5767.

[27] J. F. Matthews, M. E. Himmel, M. F. Crowley, *Cellulose* **2012**, *19*, 297.

[28] P. Chen, Y. Nishiyama, J. L. Putaux, K. Mazeau, *Cellulose* **2014**, *21*, 897.

[29] S. Y. Ding, M. E. Himmel, *J. Agric. Food Chem.* **2006**, *54*, 597.

[30] O. G. Palanna, *Engineering Chemistry*, Tata McGraw-Hill Education, New York City, New York, USA **2009**, *381*.

[31] G. R. Desiraju, *Acc. Chem. Res.* **1996**, *29*, 441.

[32] D. E. Sands, *Introduction to Crystallography*, Courier Corporation, Mineola, New York, USA **1969**.

[33] J. A. Ibers, W. C. Hamilton, *International Tables for X-ray Crystallography: Revised and Supplementary Tables*, Kynoch Press for the International Union of Crystallography, Birmingham, UK **1974**.

[34] R. J. Moon, A. Martini, J. Nairn, J. Simonsen, J. Youngblood, *Chem. Soc. Rev.* **2011**, *40*, 3941.

[35] S. Besombes, K. Mazeau, *Plant Physiol. Biochem.* **2005**, *43*, 277.

[36] C. M. Lee, J. D. Kubicki, B. Fan, L. Zhong, M. C. Jarvis, S. H. Kim, *J. Phys. Chem. B* **2015**, *119*, 15138.